A Streamline-Guided Dehomogenization Approach for Structural Design

Wang, Junpeng; Westermann, Rüdiger; Wu, J.

DOI
10.1115/1.4056148

Publication date
2023

Document Version
Final published version

Published in
Journal of Mechanical Design, Transactions of the ASME

Citation (APA)
Wang, J., Westermann, R., & Wu, J. (2023). A Streamline-Guided Dehomogenization Approach for Structural Design. *Journal of Mechanical Design, Transactions of the ASME*, *145*(2), Article MD-22-1458. https://doi.org/10.1115/1.4056148

Junpeng Wang
Computer Graphics and Visualization,
Department of Informatics,
Technical University of Munich,
Garching 85748, Germany
e-mail: junpeng.wang@tum.de

Rüdiger Westermann
Computer Graphics and Visualization,
Department of Informatics,
Technical University of Munich,
Garching 85748, Germany
e-mail: westermann@tum.de

Jun Wu[1]
Department of Sustainable Design Engineering,
Delft University of Technology,
Delft 2628 CE, The Netherlands
e-mail: j.wu-1@tudelft.nl

A Streamline-Guided Dehomogenization Approach for Structural Design

We present a novel dehomogenization approach for the efficient design of high-resolution load-bearing structures. The proposed approach builds upon a streamline-based parametrization of the design domain, using a set of space-filling and evenly spaced streamlines in the two mutually orthogonal direction fields that are obtained from homogenization-based topology optimization. Streamlines in these fields are converted into a graph, which is then used to construct a quad-dominant mesh whose edges follow the direction fields. In addition, the edge width is adjusted according to the density and anisotropy of the optimized orthotropic cells. In a number of numerical examples, we demonstrate the mechanical performance and regular appearance of the resulting structural designs and compare them with those from classic and contemporary approaches. [DOI: 10.1115/1.4056148]

Keywords: topology optimization, dehomogenization

1 Introduction

Achieving the highest stiffness while using the least amount of material is a fundamental task in mechanical design. This is often formulated as an optimization problem, e.g., topology optimization, in which the material distribution is optimized [1,2]. Early works in topology optimization employ a material model corresponding to infinitely small square cells with rectangular holes [3]. The orientation of the cell and the size of the rectangular hole therein are optimized to minimize the compliance of the structure. The material properties of these orthotropic cells are constructed using homogenization. This homogenization-based approach generates a mathematical specification of theoretically optimal structures. Yet how to translate the specification of these spatially varying orthotropic cells into a globally consistent geometry has remained a challenge. The lack of a consistent geometry means that the optimal structure is not manufacturable. To circumvent this problem, the focus of research in topology optimization has since the 1990s shifted to optimizing the distribution of solid isotropic materials. Popular approaches such as those based on density [4,5], level sets [6,7], evolutionary procedures [8], and explicit geometric descriptions [9,10], all belong to this category.

Recent years have seen a revival of homogenization-based approaches, with a focus on the post-process that translates the results of homogenization-based topology optimization into a manufacturable geometry. This post-process is now often referred to as *dehomogenization*. Special emphasis has been put on the efficient computation of a high-resolution structural design from the result of topology optimization on a coarse grid. Pantz and Trabelsi [11] proposed one of the first solutions toward this end, which was revisited and improved by Groen and Sigmund [12] and Allaire et al. [13]. These approaches have since been extended to 3D [14,15], and to deal with singularities in the optimized orientation fields [16]. It was also applied to simultaneously optimize the structural layout and the substructures therein [17]. A key component in these approaches is computing a fine-grid scalar field whose gradients are aligned with optimized orientations from homogenization-based topology optimization. Wu et al. [18] reformulated this post-process as quad/hex-dominant meshing, i.e., constructing quad/hex-dominant meshes whose edges are aligned with the optimized orientations. Stutz et al. [19] reported a method to generate high-resolution multilaminar structures from frame fields by tracing the *stream surface*. They further formulated the finding of such a set of well-spaced stream surfaces as an optimization problem. Convolutional neural networks have also been found useful for dehomogenization [20]. Alternative dehomogenization approaches include Refs. [21,22].

In the same line with previous works, we propose a dehomogenization approach that takes as input the width and orientation of spatially varying square cells that are optimized via homogenization-based topology optimization. A significant difference of our approach is that it directly generates an explicit representation in the form of a quad-dominant mesh, instead of a binary material field that needs further post-processing to translate it into a geometric representation. The edges of the mesh represent beam-like substructures of varying widths, which are aligned with the optimized cell orientations. This compact representation is beneficial for downstream operations such as user editing and fabrication process planning.

Our technical contribution is a novel method to convert the result of the homogenization-based optimization process, i.e., the optimized cell widths and orientations, into a domain-filling mesh whose elements are then dehomogenized consistently. This is achieved by first parameterizing the design domain using a set of domain-filling and evenly spaced streamlines that are aligned with the edges of optimized cells. The streamlines are then converted into a graph, from which a quad-dominant mesh whose edges follow the optimized direction fields can be computed efficiently. For dehomogenization, the edge widths are varied per element and along different directions according to the average direction and volume fraction of the optimized cells covered by an element. Thus, it can avoid the projection step to optimize for a consistent fine-grid scalar field (e.g., in Ref. [12]).

We draw inspiration from prior work on a structural design using principal stress lines (PSLs) [23–25]. The structures following principal stress directions are continuous, and this regularity is often appreciated in industrial design and architecture [26]. These prior explorations, however, make use of the principal stress directions in the stress field of a solid object with isotropic material. It deviates from the stress tensor field of the final optimized structure which is composed of orthotropic cells. Furthermore, the uniform sampling of the stress lines has been a challenge, and the beam width was

[1]Corresponding author.

Contributed by the Design Automation Committee of ASME for publication in the Journal of Mechanical Design. Manuscript received July 18, 2022; final manuscript received October 21, 2022; published online December 12, 2022. Assoc. Editor: Xu Guo.

typically assigned based on heuristics. For example, Kwok et al. [24] proposed an iterative optimization process in which lattice structures along PSLs appear incrementally. This method works for concentrated loads but it is challenging to cope with distributed loads on the design domain. Wang et al. [25] used the space-filling and evenly spaced PSLs for structural design, where the beam width was adjusted using a strain energy-based importance metric. These approaches are attractive for their computational efficiency, yet the stiffness of the obtained structures is suboptimal. In contrast to these works, we use the result of homogenization-based topology optimization for streamline tracing and to dehomogenize the single elements in the resulting mesh structure. We show that this creates structures with significantly improved stiffness.

The remainder of this paper is organized as follows. We first give an overview of the proposed method in Sec. 2. In Sec. 3, we review the problem formulation of homogenization-based topology optimization. In Sec. 4, we describe the construction process of a space-filling mesh from the direction fields that are optimized based on homogenization. Mesh-based dehomogenization is presented in Sec. 5, and we demonstrate the effectiveness of our approach in a variety of examples in Sec. 6. Section 7 concludes the paper with a discussion of the proposed approach as well as future research directions.

2 Method Overview

Our approach comprises three major stages, which are illustrated in Fig. 1. The input is a design domain including boundary conditions, i.e., the fixations of the domain and the external forces (Fig. 1(*a*)). Furthermore, the material properties and the volume fraction that can be consumed by the optimized layout are set by the user.

2.1 Optimization. In the first stage, homogenization-based topology optimization is used to optimize the orthotropic cell distribution (Fig. 1(*b*)). From this distribution, the direction fields (Fig. 1(*c*)) and the density distribution (Fig. 1(*d*)) are extracted. The direction fields locally coincide with the edges of orthotropic square cells whose deposition ratio and orientation are optimized. The size of the rectangular hole within each cell determines the local material consumption, and the ratio between the widths of the cell's edges determines the local material anisotropy.

2.2 Parametrization. In the second stage, first a domain-filling and evenly spaced set of streamlines is computed in the direction fields (Fig. 1(*e*)). Then, a graph structure is constructed, in which adjacent streamline intersection points and intersection points with the initial domain boundary are connected via edges (Fig. 1(*f*)). The graph is finally converted into a mesh that is composed of mostly quadrilateral and few triangular cells bounded by the edges of the graph (Fig. 1(*g*)).

2.3 Dehomogenization. In this last stage, the final structural design (Fig. 1(*h*)) is computed by jointly using the quad-dominant mesh, the optimized density distribution, and the anisotropy of optimized square cells. The mesh structure divides the design domain into a space-filling set of elements whose interior is filled with material according to the optimized density distribution and the anisotropy of each element.

3 Homogenization-Based Topology Optimization

For structures under a single load, the theoretically optimal structural layout can be approximated by optimizing the distribution of square cells with a rectangular hole [3]. As illustrated in Fig. 2(*a*), the design domain is discretized into finite elements. Each element represents a repetition of an adapted configuration of the unit cell. The square cell has a unit side length. Within it, there is a rectangular hole (Fig. 2(*c*)). The configuration of the unit cell is thus described by the hole sizes α_x and α_y and rotation angle θ. The mechanical properties of the unit cell are orthotropic. In this paper, we refer to these adapted cells as *orthotropic cells*. The density or deposition ratio (ρ_e) of each cell is measured by $1-\alpha_x\alpha_y$. The elasticity tensor of the orthotropic cell is computed by

$$C(\alpha_x, \alpha_y, \theta) = R^T(\theta)C^H(\alpha_x, \alpha_y)R(\theta) \tag{1}$$

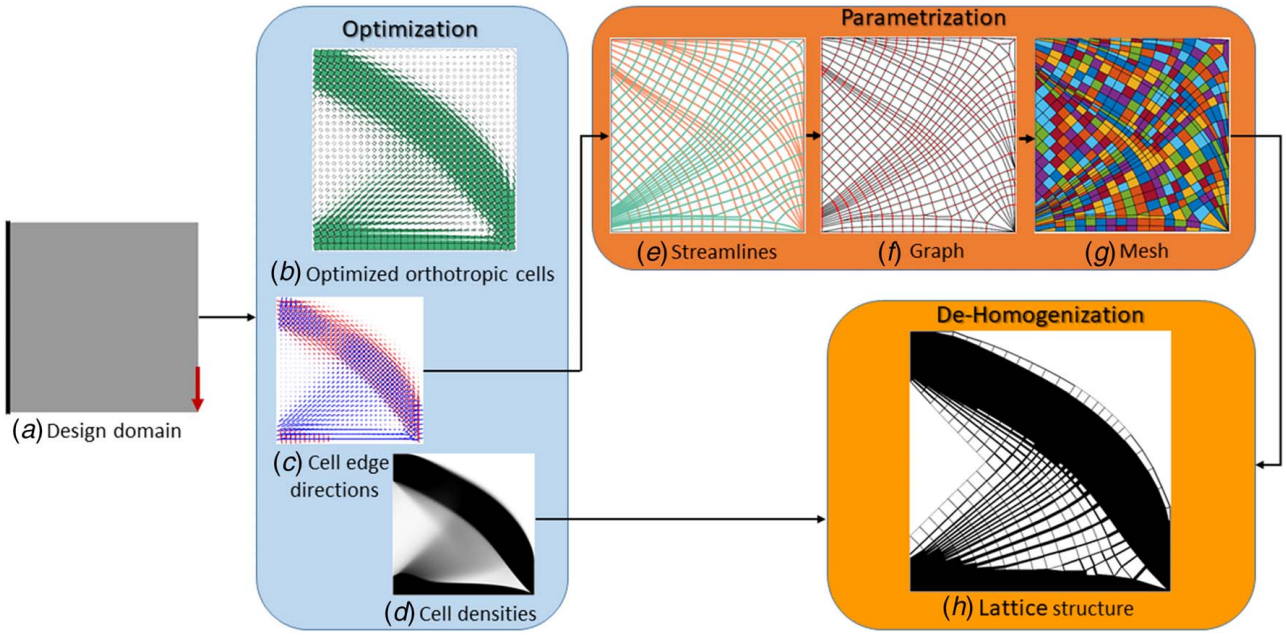

Fig. 1 Method overview. (*a*) The design domain and boundary conditions. (*b*) The optimized distribution of orthotropic cells from homogenization-based topology optimization. (*c*) The mutually orthogonal direction fields defined by the axes of the orthotropic cells. (*d*) The equivalent density distribution of the orthotropic cells. (*e*) Streamlines traced along the two orthogonal direction fields. (*f*) The graph structure extracted from the streamlines. (*g*) The quad-dominant mesh obtained from the graph structure. (*h*) The final structural design.

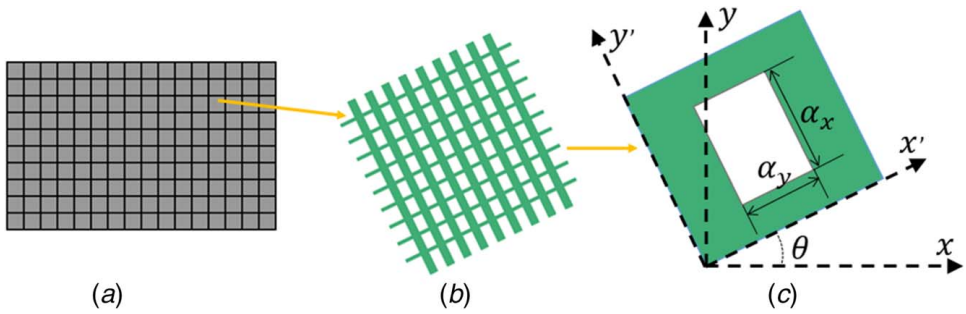

Fig. 2 (*a*) The design domain is discretized into bilinear square grids. (*b*) Each square element is assumed to be filled by the orthotropic material. (*c*) The size and orientation of the approximately equivalent orthotropic cell, i.e., the square element with a rectangular hole, are taken as design variables in homogenization-based topology optimization.

where $R(\theta)$ is the rotation matrix, and $C^H(\alpha_x, \alpha_y)$ represents the effective elasticity tensor for an axis-aligned unit cell with α_x, α_y, evaluated by homogenization.

The structural design is formulated as compliance minimization

$$\min_{\boldsymbol{\alpha}_x, :\boldsymbol{\alpha}_y, :\boldsymbol{\theta}} \quad \frac{1}{2}\boldsymbol{F}^T\boldsymbol{U} \tag{2}$$

$$\text{subject to} \quad \boldsymbol{K}(\boldsymbol{\alpha}_x, :\boldsymbol{\alpha}_y, :\boldsymbol{\theta})\boldsymbol{U} = \boldsymbol{F} \tag{3}$$

$$\frac{1}{n}\sum_e \rho_e - \alpha_{global} \leq 0 \tag{4}$$

$$0 \leqslant \alpha_x, :\alpha_y \leqslant 1 \tag{5}$$

Here the objective is to minimize the elastic energy. $\boldsymbol{F}$ is the loading vector. $\boldsymbol{U}$ is the displacement vector, obtained by solving the static equilibrium equation (Eq. (3)). $\boldsymbol{K}$ is the stiffness matrix in finite element analysis. n is the number of finite elements. α_{global} is the volume fraction prescribed by the user.

We use the procedure reported by Groen and Sigmund [12] for solving the optimization problem. The educational code for this was provided in the review article [27]. In this procedure, α_x and α_y are optimized by gradient-based numerical optimization, while the rotation angle (θ) in each iteration is determined by the corresponding principal stress direction.

Figure 3 demonstrates the results of the homogenization-based optimization for the "Cantilever" model, showing the initial domain and external forces (*a*), the extracted density layout (*b*), and the direction fields of the optimized orthotropic cell distribution (*c*). Figure 3(*d*) provides a closeup view of the layout of the orthotropic cells. This layout is not directly manufacturable and needs to be transformed into a consistent geometry.

4 Parametrization

The goal of our approach is to convert the locally spatial-varying orthotropic cells into a globally consistent geometry. While thick substructures or one single solid block should be placed in dense regions, in less dense regions only few thin substructures are required. These substructures follow the optimized direction fields. In contrast to previous approaches that find a fine-grid scalar field with constraints on its gradient, we trace streamlines along the optimized direction fields. This ensures a global consistency of the substructures and their alignment with the optimized direction fields.

We use the direction fields that are optimized via the homogenization-based approach and generate a trajectory-based parametrization of the design domain. Therefore, a uniformly distributed set of streamlines in the direction fields is computed by using the stress tensor visualization tool by Wang et al. [28]. It enables to compute and visualize a space-filling and evenly spaced set of streamlines in three mutually orthogonal direction fields. By setting the third vector field to zero, it can be used right away to work with 2D fields (i.e., the *u*- and *v*-field in our current application). We will subsequently call the corresponding streamlines in the *u*- and *v*-field the *u*-streamlines and *v*-streamlines, respectively. The streamline seeding strategy ensures that around each streamline an empty band is generated from which no streamline is seeded, and new streamlines are always seeded from points on existing streamlines. In this way, a fairly uniform and space-filling set of streamlines is computed (see Fig. 4(*a*)).

Each streamline can be converted into a polyline consisting of a set of intersection points and linear connections between them [29]. From this representation, a graph structure with the nodes and edges, respectively, being the intersection points and piecewise linear connections between them can be easily constructed. By connecting adjacent integration points on the domain boundaries, the final graph—due to the mutual orthogonality of the *u*- and *v*- streamlines—comprises mostly regions that are bounded by exactly four edges. Only at degenerate points and at points lying on a boundary, regions that are bounded by three edges can occur. The result of this process is shown in Fig. 4(*b*).

Finally, the graph structure is used to discretize the design domain into a set of independent elements, i.e., the interior regions of the graph structure, so that each element can be dehomogenized independently. The orientation of the elements is given by

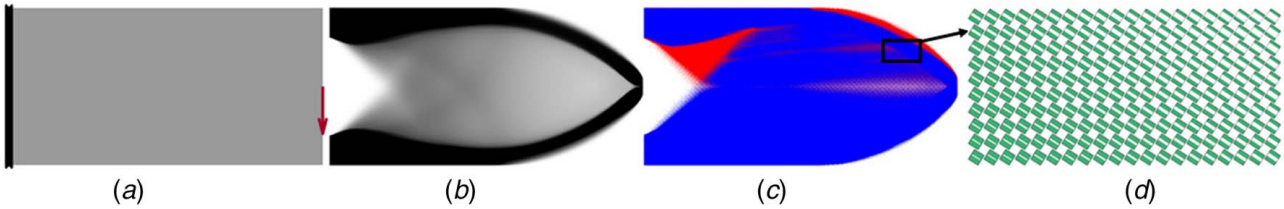

Fig. 3 (*a*) The design domain. (*b*) and (*c*) The optimal density layout and the corresponding direction field produced by the homogenization-based optimization. (*d*) Closeup of the optimized orthotropic cells sampled from the highlighted region in (*c*).

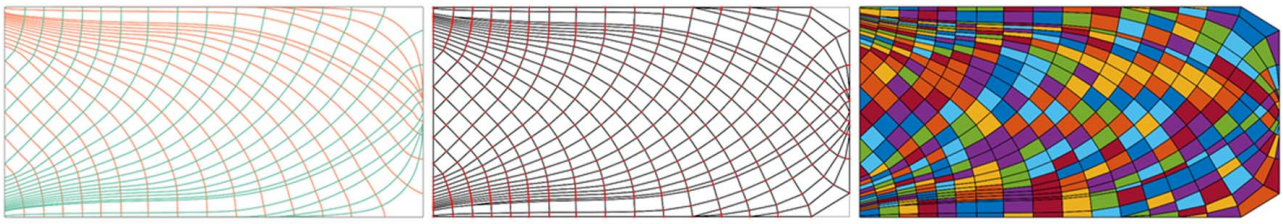

Fig. 4 Parametrization by streamlines. (*a*) Space-filling and evenly spaced streamlines. (*b*) Graph structure. (c) Quad-dominant mesh.

the streamline skeleton, and the dehomogenization process proceeds by filling the elements with material according to the optimized density field. This is performed by extruding material from the edges of each element inward, according to the volume fraction of the continuous density field in each element. To do so, the graph structure first needs to be converted into an explicit cell-based mesh structure.

Since the 2D graph structure represents the connectivity (i.e., the edges) between the coordinates of the streamline intersection points, a quad-dominant mesh can be constructed in a straightforward way from this structure. By iteratively processing the local vertex and edges topology along streamlines, a mesh comprising quadrilateral and triangular elements can be computed, along with the cell topology that represents the cell adjacency information. Note that the local ordering of nodes of each quadrilateral and triangular cell needs to be consistent, i.e., either clockwise or counter-clockwise. Figure 4(*c*) shows the constructed mesh from the graph structure in Fig. 4(*b*).

4.1 Singularities. To obtain a consistent mesh structure from the streamline skeleton, singularities in the direction fields need to be determined and treated in a special way. In our case, where the direction fields coincide with principal stress directions, singularities occur at so-called degenerate points of the corresponding stress field, i.e., points where the two eigenvalues of the stress tensor in the underlying stress tensor field become indistinguishable. In the seminal work by Delmarcelle and Hesselink [30] both the classification of degenerate points and their numerical computation are discussed. In the vicinity of degenerate points, a set of hyperbolic and parabolic sectors exist, in which similar patterns of neighboring trajectories are observed. The topological skeleton consists of the boundaries between adjacent sectors—so-called separatrices—and indicates pathways along which the forces are steered toward the degenerate points. By first extracting the degenerate points and computing the topological skeleton, the separatrices can then considered as seed streamlines as described before, so that an evenly spaced set of streamlines is computed in each sector. Let us refer to the work by Wang et al. [29] for a more detailed description of the implemented procedure. Figures 11(*b*) and 13(*f*) show the embedding of singularities into the computed streamlines.

5 Dehomogenization

In order to dehomogenize the optimal density layout, i.e., to convert the continuous density layout into a binary one, we utilize the constructed quad-dominant mesh and dehomogenize the region covered by each mesh element separately. As shown in Fig. 5, each element covers a certain region in the domain. The material in each region, i.e., the deposition ratio, should be re-distributed so that (a) a binary material layout is generated, (b) a continuous transition at the element boundaries is obtained, and (c) the orthotropic cells' orientations, which have been optimized with respect to the object's compliance, is reflected in the binary material layout. The target deposition ratio v_i^* of a mesh element (see Fig. 5) is measured by D/M, where M is the number of orthotropic cells located in the region covered by the element, and D is the sum of the density values over all these cells. The dehomogenized mesh element should keep this deposition ratio after dehomogenization.

Our approach can generate the final design at different granularity levels in a straightforward way, by varying the width of the empty bands around each computed streamline. The width is controlled by the distance threshold in the streamline seeding process (refer to Ref. [28] for details). Since the resolution of the corresponding quad-dominant mesh varies spatially and is not necessarily at a resolution comparable to the finite element discretization used in topology optimization, the density and directions need to be resampled from the finite element grid to compute the target deposition ratio of a mesh element. This is performed via bi-linear interpolation at a set of sampling points in each mesh element.

5.1 Anisotropic Mesh Element. To distribute the material in a mesh element according to the mentioned requirements, we propose to extrude the available material from the edges of each element inward. By starting with a minimal edge thickness, the edges are iteratively thickened until all available material is used. In this way, we enforce a layout that aligns with the element orientation, seamlessly connects adjacent elements, and can furthermore account for an anisotropic stress distribution by adapting the edge thickness according to the mechanical properties of each element.

The process starts by removing mesh elements that have a very low target deposition ratio (e.g., $v^* < 0.05$), in order to avoid the generation of very thin mesh edges that can cause difficulties in the manufacturing process. Similarly, mesh elements with a large deposition ratio (e.g., $D/M > 0.95$) are made fully solid. The edges of all remaining mesh elements are set to a minimum thickness t_0.

Taking a single mesh element as shown in Fig. 6, its deposition ratio v is computed as the sum of the areas A_i covered by each extruded edge, subtracting the subareas that are counted twice, and then dividing by the total area of the element. We start with two opposite edges and compute for each edge the intersection points between the extruded edge and the respective other mesh edges (P_{00}, P_{01}, P_{20}, P_{21} in Fig. 6). Including the endpoints of the mesh edges, this gives two quadrilaterals A_0, A_2, whose areas can be computed via triangulation. For the other two mesh edges, we

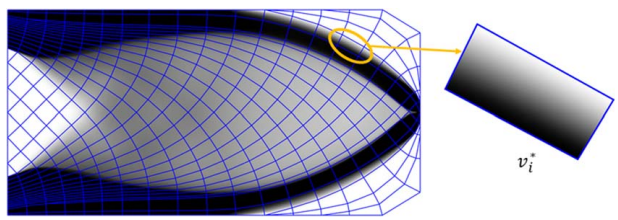

Fig. 5 Correspondence between continuous material field and mesh elements, facilitating the assignment of a material budget v_i^* to each mesh element and dehomogenization of each element separately

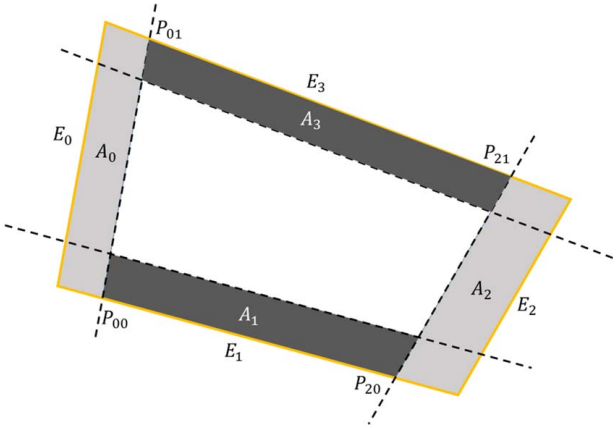

Fig. 6 Schematics of computing the area subtended by edges of a certain thickness. From intersection points between dashed lines (extruded edges) and edges of the mesh element the areas can be computed.

use the newly computed edge intersection points and the intersection points between the four extruded edges and compute two quadrilaterals representing the missing areas A_1, A_3. Now, the thickness t of each edge can be increased iteratively from the initial value t_0, until the actual deposition ratio v approaches the target v^*, i.e., the available material budget is used.

In order to match the mechanical properties of the set of orthotropic cells covered by a single mesh element, we start with a minimal edge thickness and then thicken the edges according to the ratio of the edge thicknesses of the orthotropic cells (Fig. 7). The edge thicknesses $1-\alpha_x$ and $1-\alpha_y$ as well as the orientation of an orthotropic cell have been optimized to maximize the stiffness of the resulting layout. As such, if all cells covered by a mesh element have the same thickness ratio, and are consistently orientated with the mesh element, the material should be deposited along the element edges so that the thickness ratio of the cells is maintained. However, since the ratio and orientation vary across the cells, in general, we first need to compute representative values for both (see Fig. 7 bottom for an illustration).

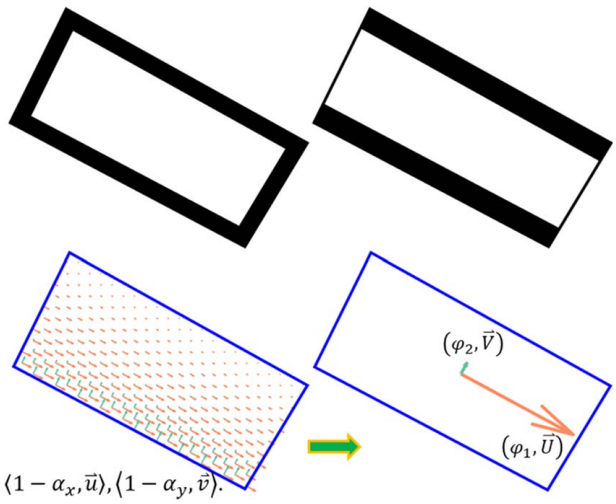

Fig. 7 Top: The edges are equally thickened (left) or thickened (using the same amount of material) according to the edge thicknesses of the orthotropic cells they cover (bottom left). Bottom: For the set of orthotropic cells covered by a mesh element, representative edge thicknesses and orientation are computed via averaging. The arrow length indicates the thickness of edges along the pointing direction.

We do so by first computing the normalized thickness of the cell edges φ_1 and φ_2 following the u- and v-field, respectively, by adding up the values of the per-cell thicknesses and dividing through the maximum of the resulting values, i.e.,

$$\varphi_1^* = \sum (1-\alpha_x^i), \ :\varphi_2^* = \sum (1-\alpha_y^i)$$
$$\varphi_1 = \frac{\varphi_1^*}{\max(\varphi_1^*, \varphi_2^*), \varphi_2} = \frac{\varphi_2^*}{\max(\varphi_1^*, \varphi_2^*)} \tag{6}$$

Then, to determine which edge of the mesh element corresponds to φ_1 and which to φ_2, we compute the average direction vectors $\vec{U}$ and $\vec{V}$ of all the per-cell direction vectors $\vec{u_i}$ and $\vec{v_i}$, i.e., $\vec{U} = \text{norm}(\sum \vec{u_i})$ and $\vec{V} = \text{norm}(\sum \vec{v_i})$. We let the mesh edges correspond to $\vec{U}$ or $\vec{V}$ to which they have the least directional deviation.

Now, we can introduce for each mesh edge e_j a scaling factor w_j, which is calculated by $e_j = t_0 + w_j\delta$. Here δ is an increment used for adjusting the edge thickness iteratively. With the thicknesses and directions $(\varphi_1, \vec{U})$ and $(\varphi_2, \vec{V})$, the corresponding weighting factor w_j of the jth element edge is given by

$$w_j = \begin{cases} \varphi_1 & \theta_{j1} \leqslant \theta_{j2} \\ \varphi_2 & \theta_{j1} > \theta_{j2} \end{cases} \tag{7}$$

Here, θ_{j1} and θ_{j2} are the included angles between the jth element edge and the directions $\vec{U}$ and $\vec{V}$, respectively, and we consistently use the same thickness for opposite edges in each quadrilateral element, and the triangular elements are treated as degenerate quadrilaterals where one of the edges is collapsed, specifically, for each edge, the weighting factor w_j is determined by Eq. (7).

It is worth mentioning that in rare cases the per-cell directions may change considerably in a single mesh element, and thus the per-element direction becomes less representative. To cope with this, the mesh element can be subdivided into a set of smaller elements, for each of which the dehomogenization is performed as described.

6 Results

We demonstrate our dehomogenization approach with several examples and compare the results to those of density-based and dehomogenization approaches. In all cases, the design domains are discretized by Cartesian grids with unit-size. Young's modulus and Poisson's ratio are set to 1.0 and 0.3, respectively. Homogenization-based topology optimization is performed with the MATLAB code provided in Ref. [27]. We terminate the optimization process after 200 iterations. We have implemented the proposed parametrization and dehomogenization operations in MATLAB as well. All experiments have been carried out on a desktop PC with an Intel Xeon CPU at 3.60 GHz.

6.1 Comparison to Density-Based Approaches. In our first experiment, we use the cantilever model described in Fig. 3(*a*) to demonstrate the properties of the proposed dehomogenization approach and compare the results to those of density-based topology optimization.

Figure 8 (top) shows the dehomogenization results for different streamline densities, resulting in an increased or decreased number of ever smaller or larger mesh elements, respectively. The compliances of the designs with different granularity vary only slightly. With c_0 being the compliance of the fully solid domain, one can see that with the same amount of material all resulting designs achieve almost the same compliance of roughly $1.5c_0$. The compliance of the dehomogenized binary layouts is slightly higher than that from homogenization-based optimization ($1.447c_0$).

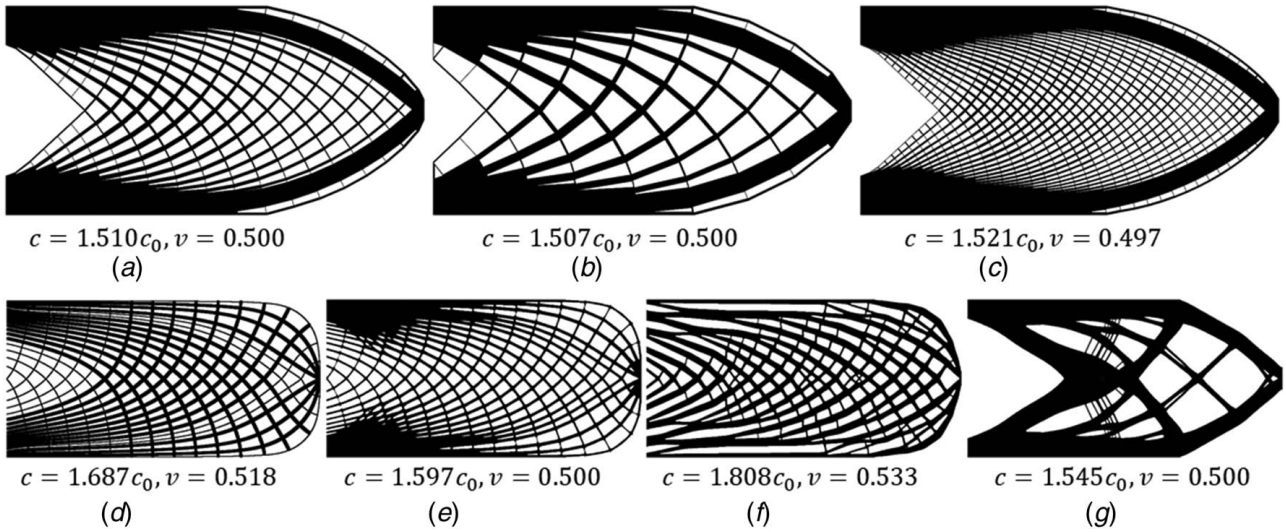

Fig. 8 Top: Results with the proposed dehomogenization strategy. (*a*)–(c) demonstrate the changes due to different amounts of streamlines used in the parametrization stage. Bottom: Comparison to alternative approaches for generating a binary design via topology optimization. (*d*) PSL-guided material layout [25]. (e) PSLs-initialized density-based topology optimization using a global volume constraint [25]. (*f*) Porous-infill optimization with local volume constraints [31]. (*g*) Density-based topology optimization with a global volume constraint. c_0 and c, respectively, are the compliances of the fully solid domain and the shown results, and *v* is the volume fraction.

In Fig. 8 (bottom), we compare our results to those generated by the stress trajectory-guided structural design by Wang et al. [25], the porous-infill approach using local volume constraints by Wu et al. [31], and density-based topology optimization with a global volume constraint. In all examples, the same number of simulation element as for dehomogenization in our approach is used.

Figures 8(*d*) and 8(*e*) show the results of stress trajectory-guided structural design. In (*d*), the material is distributed along principal stress trajectories of the solid object under load, and the thickness of the material is adapted according to the accumulated strain energy along each trajectory. Figure 8(*e*) shows the optimized material layout when the material field in (*d*) is used as initialization for topology optimization with a global volume constraint. The generated layouts also show a very regular structural design, but a considerably higher compliance than the dehomogenization approach. The latter can also be observed when comparing to porous infill optimization (Fig. 8(*f*)) which applies a strict constraint on a local volume. Here, besides having a smaller compliance, the dehomogenized layout (Figs. 8(*a*)–8(*c*)) also shows a more regular structural layout. Notably, while porous-infill optimization generates many bifurcations, i.e., solid strands that merge and split, the dehomogenization approach, per construction, results in a grid-like structure mostly comprising quadrilateral elements. Finally, compared to density-based topology optimization with a global volume constraint (Fig. 8(*g*)), our result still shows a slightly smaller compliance, yet the results are far more regular and, are expected to exhibit higher stability when the load conditions are changed or certain parts undergo damage, as demonstrated for evenly spaced, space-filling structures in Refs. [29,31].

6.2 Comparison to Dehomogenization Approaches. A major difference between our approach and previous dehomogenization approaches (e.g., Refs. [12,13]) is the representation of the optimized structure. Our design is encoded by a graph, rather than a density distribution. The graph-encoded representation is more convenient for downstream operations such as user editing and fabrication tool-path generation, though these advantages are not explored further here.

In Fig. 9, we compare the result that is obtained with our approach to the result of projection-based dehomogenization by Groen and Sigmund [12]. To match their model configuration, the force applied to the cantilever model has been changed accordingly, and homogenization-based topology optimization is performed at a coarse grid resolution of 100×50. Density-based topology optimization using a global volume constraint is also included here as a reference. It is computed at a grid resolution of 1600×800. It can be seen that the compliance of the layout generated by our approach (*d*) is only slightly higher than that of the layout produced by the method of Groen and Sigmund in (*e*), yet using a little less material. The layout in (*e*) has some concentrated clusters in the middle of the

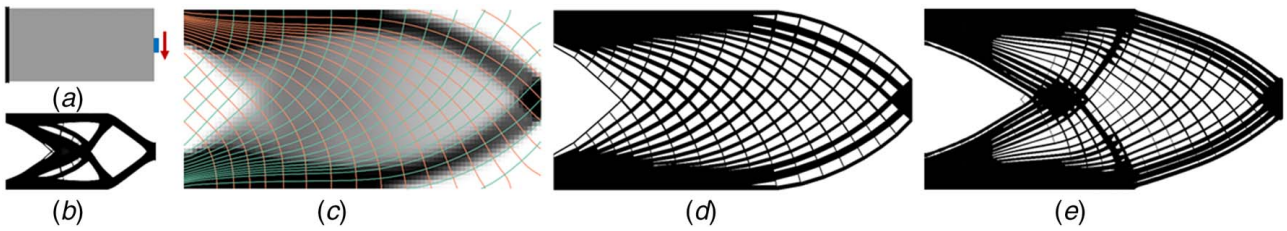

Fig. 9 Comparison of dehomogenization approaches on a cantilever beam. (*a*) The design domain and boundary conditions. (*b*) The result of density-based topology optimization with a global volume constraint simulated ($c = 62.56$, $v = 0.500$). (c) Optimal density layout ($c = 57.21$, $v = 0.500$), superimposed with streamlines. (*d*) The dehomogenized structural design by our method ($c = 60.04$, $v = 0.500$). (e) The result of the projection-based dehomogenization ($c = 58.57$, $v = 0.510$). The image (e) is reprinted from Ref. [12] with permission from *John Wiley & Sons*.

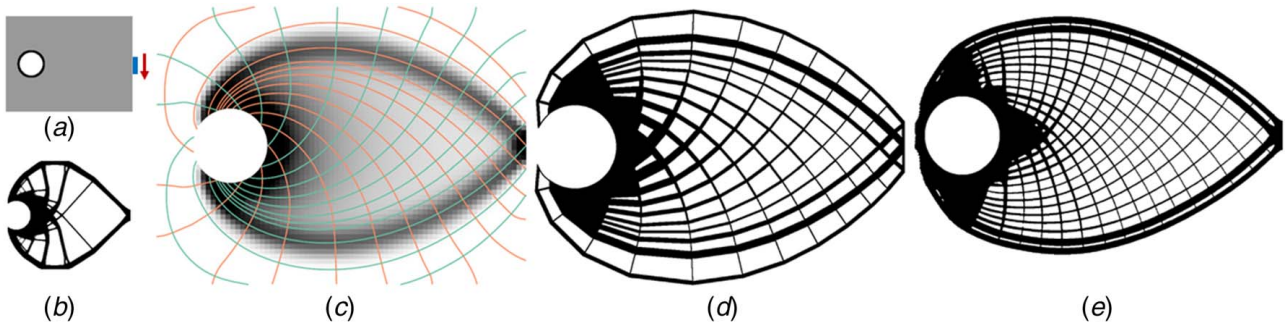

Fig. 10 Comparison of dehomogenization approaches on Michell's structure. (*a*) The design domain and boundary conditions. (*b*) The result of density-based topology optimization with a global volume constraint ($c = 64.452$, $v = 0.250$). (c) Optimal density layout ($c = 55.64$, $v = 0.250$), superimposed with streamlines. (*d*) The dehomogenization using our approach ($c = 62.301$, $v = 0.250$). (*e*) The result of the projection-based dehomogenization ($c = 67.830$, $v = 0.252$). The image (*e*) is reprinted from Ref. [12] with permission from *John Wiley & Sons*.

domain, while our approach generates a more uniform grid-like material layout. This difference is likely due to the parameter setting (e.g., the filter size) in the homogenization-based topology optimization. While Groen et al. perform an optimization to generate a consistent binary pattern at finer resolution (1600×800 in the example) from the coarse grid results, in our method the resolution of the final layout is controlled by the density of seeded streamlines. Since streamlines are always traced in the initial domain, they always stay entirely within the domain. The optimized quantities required to trace streamlines and dehomogenize the final mesh elements are reconstructed via bilinear interpolation from the coarse grid.

Figure 10 shows the structural design that is generated by our method when applied to Michell's structure according to the specification in Ref. [12]. The coarse and fine grid resolutions used for optimization and dehomogenization are 80×60 and 1280×960, respectively. As can be seen, perfect symmetry is not achieved, because the streamline seeding process does not consider symmetry in the design domain or the underlying direction field. If symmetry is known beforehand, however, the seeding process can be adapted accordingly. The compliance of the streamline-guided design (Fig. 10(*d*)) is even lower than the design that is generated via projection-based dehomogenization (Fig. 10(*e*)). Overall, our experiments indicate that streamline-based dehomogenization generates designs with a compliance that is comparable to what can be achieved with a projection-based approach.

6.3 Performance Analysis. Our proposed strategy can be split into *parametrization* and *dehomogenization*. In the parametrization stage, it is first required to compute a set of domain-filling and evenly spaced streamlines. Under the assumption that the streamline density is selected so that the initial seed points are about a distance of one cell size from each other, the computational complexity is

Table 1 Quality and timing statistics for streamline-guided dehomogenization

Examples	c ($\cdot c_0$)	c^* ($\cdot c_0$)	c^+ ($\cdot c_0$)	ξ ($\frac{c-c^*}{c^*} \times 100\%$)	Streamlines	Elements	t_1 (s)	t_2 (s)	t_3 (s)	t_4 (s)	T (s)
Square (Fig. 1(*h*))	1.261	1.242	1.276	1.53%	57	647	0.85	2.46	3.74	2.17	9.22
Cantilever 1 (Fig. 8(*a*))	1.510	1.447	1.545	4.35%	46	464	0.76	2.24	3.66	1.50	8.16
Cantilever 2 (Fig. 11(*c*))	1.170	1.138	1.156	2.81%	66	574	1.34	3.31	4.83	1.83	11.31
Cantilever 3 (Fig. 12(*d*))	1.661	1.533	1.675	8.35%	40	416	0.70	1.68	3.25	1.61	7.24
Cantilever 4 (Fig. 9(*d*))	1.564	1.493	1.629	4.76%	40	376	0.63	1.40	3.13	1.55	6.71
Michell's structure (Fig. 10(*d*))	3.176	2.837	3.286	11.95%	32	198	0.41	0.79	1.24	1.23	3.67
L-shaped beam (Fig. 13(*c*))	1.397	1.332	1.399	4.88%	58	504	0.75	2.04	1.65	1.58	6.02
Double-clamped beam (Fig. 13(*g*))	1.763	1.663	1.808	6.01%	55	396	1.61	1.37	2.14	1.65	6.77

Note: c^* and c, respectively, are the compliance of the optimal layout resulting from homogenization-based topology optimization and after streamline-guided dehomogenization. ξ measures the deviation. c^+ is the compliance by conventional topology optimization with a global volume fraction constraint.#Streamlines and#Elements refer to the number of the used streamlines, and the number of resulting mesh elements, respectively. t_1 and t_2 are the times for streamline generation and mesh construction (incl. graph extraction) during parametrization, respectively. t_3 and t_4 are the times for computing the available material budget for each mesh element and the edge thicknesses during dehomogenization, respectively. T is the overall time.

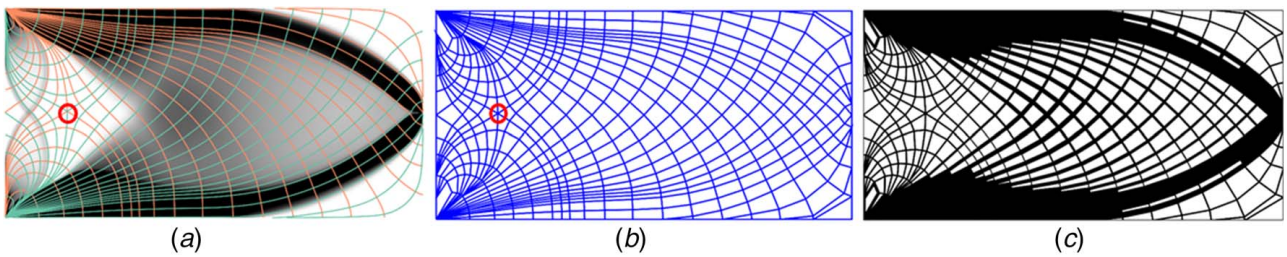

Fig. 11 Tests on a cantilever beam fixed by the endpoints of its left boundary. (*a*) Optimal density layout ($c^* = 1.138c_0$, $v = 0.500$) and streamlines. (*b*) The generated streamline graph. The degenerate point (singularity) is marked by a circle. (c) The dehomogenized structural design ($c = 1.170c_0$, $v = 0.500$).

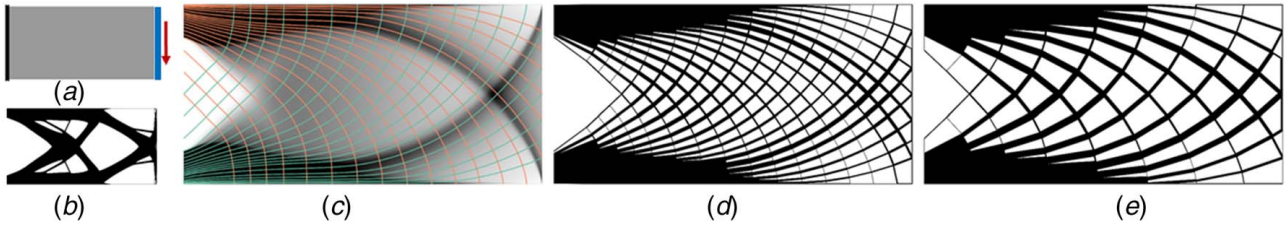

Fig. 12 (*a*) A cantilever under a distributed load along the right edge. (*b*) Result of density-based topology optimization with a global volume constraint ($c = 1.675c_0$, $v = 0.500$). (*c*) Optimal density layout ($c^* = 1.533c_0$, $v = 0.500$) and streamlines. (*d*) Dehomogenized structural design ($c = 1.661c_0$, $v = 0.500$). (*e*) Dehomogenized structural design with less streamlines ($c = 1.680c_0$, $v = 0.500$).

$O(N)$, where N is the number of cells. In addition, whenever a new streamline is computed, all remaining seed points within a band of a selected width around that streamline are discarded. Since this band can be represented in the grid structure by flagging cells entirely outside the band, this operation requires to investigate only few of all possible seed points. Finally, to generate a mesh structure, the intersections between the streamlines along one optimized direction field with all other streamlines of the respective other direction field need to be computed. A straightforward realization is to first compute all intersection points, including the indices of the intersecting streamlines, to store them in a shared point representation, and then sort these points along each streamline

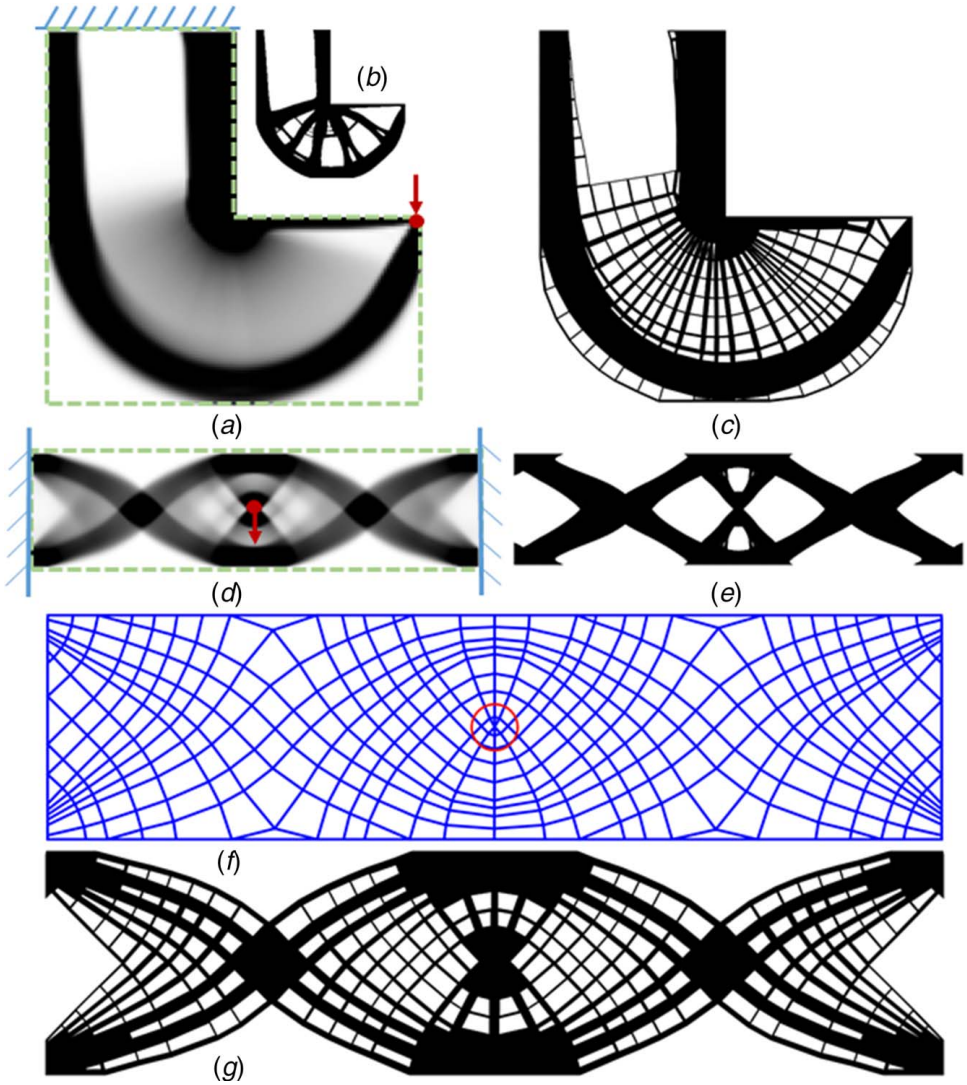

Fig. 13 (*a*) Optimal density layout ($c^* = 1.332c_0$, $v = 0.500$) for an L-shaped beam under a point load. (*b*) Inlet shows the binary result of density-based topology optimization with a global volume constraint ($c = 1.399c_0$, $v = 0.500$). (*c*) Dehomogenization result ($c = 1.397c_0$, $v = 0.500$). (*d*) Optimal density layout ($c^* = 1.663c_0$, $v = 0.500$) for a double-clamped beam. (*e*) Binary result of density-based topology optimization with a global volume constraint ($c = 1.808c_0$, $v = 0.500$). (*f*) Streamline graph used for dehomogenization. A degenerate point is marked by a circle. (*g*) Dehomogenization result ($c = 1.763c_0$, $v = 0.500$).

individually. Notably, intersection computations and sorting can be parallelized effectively, so that we even expect interactive update rates for the grid resolutions used in our work when using an optimized GPU solution.

In the dehomogenization stage, it is first required to determine the target deposition ratio v_i^* of each mesh element, and then to compute the widths of the element edges to enforce the same deposition ratio before and after dehomogenization. Notably, since the mesh elements can be processed independently, also this process can be effectively parallelized.

In contrast to our approach, previous dehomogenization approaches (e.g., Refs. [12,13]) require solving a linear system of equations with as many degrees of freedom as cells on the finest level. Even with optimized solvers, the number of iterations is of the order N and, thus, computationally more demanding than our approach. As an indication of improved computational complexity, our approach took 10 s or less for most of the examples, while in Ref. [12] under the same problem settings the computations took 100 s. The computers used for testing were not precisely the same but comparable.

Table 1 provides a performance and quality assessment of all examples used in this work, including the compliances of the dehomogenized designs (c), the deviations (ξ) to the homogenization-based analysis (c^*), the number of used streamlines, the number of elements of the generated mesh, and the corresponding computation times. We further split the computation times required by parametrization into streamline generation (t_1) and mesh construction (t_2), and the times required by dehomogenization into the target deposition ratio calculation (t_3) and edge width identification (t_4). In all of our experiments, the time for parametrization and dehomogenization combined is about 10 s or even less. We also list the compliance (c^+) of the results that are generated by topology optimization with a global volume constraint under the same design specifications.

6.4 Singularity Treatment. As we described in Sec. 4, our proposed approach can handle situations where singularities exist in the direction fields that are obtained via homogenization-based optimization. Such singularities usually incur discontinuities during streamline tracing, and they furthermore result in low convergence for density-based topology optimization under local volume constraints [29]. The singularity can be detected by topology analysis of the orthogonal direction fields. As an example, we again use the cantilever model (Fig. 3(*a*)), but now replace the distributed fixation condition with point fixations applied on the endpoints of the left boundary. Figure 11(*a*) highlights a singularity in the left part of the domain, where three u-streamlines and three v-streamlines converge to a single point. This type of singularity is termed a trisector degenerate point in stress topology analysis, and the six streamlines are the corresponding topological skeleton. Figure 11(*b*) shows the generated mesh, which demonstrates that a consistent structure can be obtained around the singularity. The dehomogenized result is shown in Fig. 11(*c*).

6.5 Distributed Loads. Our dehomogenization approach naturally works well also for distributed loads. Figure 12(*a*) shows the structural design problem under distributed loads. Figure 12 compares the results of density-based topology optimization with a global volume constraint to those of our proposed dehomogenization method using different streamline densities. The compliance from density-based topology optimization is between the tight range of compliances of dehomogenized structures with two different streamline densities. The deviation of the compliances of the dehomogenized structures ((*d*) and (*e*)) from the compliance in homogenization (*c*) is less than 10%.

6.6 L-Shaped Beam and Double-Clamped Beam. We have also tested our approach on an L-shaped beam and a double-clamped beam. Figure 13 shows the optimized results. In both cases, the compliance of the dehomogenized layout is about 5% higher than the compliance after homogenization. It is worth noting that also in the stress field of the double-clamped beam a degenerate point occurs, which, according to the topological skeleton, generates a grid composed of triangular and quadrilateral mesh elements around it. In these two examples, as in previous examples, the compliance of the dehomogenized structure is lower than that from the density-based approach with a global volume constraint.

7 Conclusion and Future Work

In this paper, we have introduced a novel streamline-based parametrization of a design domain to dehomogenize the optimal continuous density layout produced by homogenization-based topology optimization. The compliance of the dehomogenized high-resolution structures is very close to that of the optimal design from homogenization-based optimization, and it is consistently superior to the compliance achieved via density-based topology optimization. The resulting structures exhibit a globally regular appearance, uniformly covering the domain with quad-dominant mesh elements.

In the current work we did not strive for an efficient implementation of the method. However, streamline integration and intersection computation can be effectively parallelized, for instance, on a GPU. The intersection points are already ordered along the streamlines, and graph as well as mesh construction requires only local access operations to adjacent streamlines or intersection points. Thus, we believe that the entire approach can be implemented on the GPU so that even instant dehomogenization is possible once the continuous density layout is available. We will consider such an implementation in future work and investigate the possibility for designers to probe different streamline densities and seeding strategies. We will also investigate post-processing techniques, either automatic or with user interaction, e.g., to remove sparse thin layers that correspond to low stiffness regions (see Fig. 11 left middle, top right, and bottom right). Finally, we are particularly interested in extending this approach to design 3D beam-like lattice structures. A challenge here is that the intersection of independently traced streamlines in 3D happens only coincidentally. A possible solution is to locally relax the streamline alignment, e.g., using field-guided hex-dominant meshing [18,32]. An alternative solution is to explore the optimization approach for constructing stream surfaces [19].

Acknowledgment

This work was supported by the German Research Foundation (DFG) under Grant No. WE 2754/10-1.

Conflict of Interest

There are no conflicts of interest.

Data Availability Statement

The authors attest that all data for this study are included in the paper.

References

[1] Bendsøe, M., and Sigmund, O., 2004, *Topology Optimization: Theory, Methods, and Applications*, Springer, Berlin, Heidelberg

[2] Sigmund, O., and Maute, K., 2013, "Topology Optimization Approaches," Struct. Multidiscip. Optim., **48**(6), pp. 1031–1055.

[3] Bendsøe, M. P., and Kikuchi, N., 1988, "Generating Optimal Topologies in Structural Design Using a Homogenization Method," Comput. Methods Appl. Mech. Eng., **71**(2), pp. 197–224.

[4] Bendsøe, M. P., 1989, "Optimal Shape Design As a Material Distribution Problem," Struct. Optim., **1**(4), pp. 193–202.

[5] Sigmund, O., 2001, "A 99 Line Topology Optimization Code Written in Matlab," Struct. Multidiscipl. Optim., **21**(2), pp. 120–127.

[6] Wang, M. Y., Wang, X., and Guo, D., 2003, "A Level Set Method for Structural Topology Optimization," Comput. Methods Appl. Mech. Eng., **192**(1), pp. 227–246.
[7] Allaire, G., Jouve, F., and Toader, A.-M., 2004, "Structural Optimization Using Sensitivity Analysis and a Level-Set Method," J. Comput. Phys., **194**(1), pp. 363–393.
[8] Xie, Y., and Steven, G., 1993, "A Simple Evolutionary Procedure for Structural Optimization," Comput. Struct., **49**(5), pp. 885–896.
[9] Norato, J., Haber, R., Tortorelli, D., and Bendsøe, M. P., 2004, "A Geometry Projection Method for Shape Optimization," Int. J. Numer. Methods Eng., **60**(14), pp. 2289–2312.
[10] Guo, X., Zhang, W., and Zhong, W., 2014, "Doing Topology Optimization Explicitly and Geometrically—A New Moving Morphable Components Based Framework," ASME J. Appl. Mech., **81**(8), p. 081009.
[11] Pantz, O., and Trabelsi, K., 2008, "A Post-Treatment of the Homogenization Method for Shape Optimization," SIAM J. Control Optim., **47**(3), pp. 1380–1398.
[12] Groen, J. P., and Sigmund, O., 2018, "Homogenization-Based Topology Optimization for High-Resolution Manufacturable Microstructures," Int. J. Numer. Methods Eng., **113**(8), pp. 1148–1163.
[13] Allaire, G., Geoffroy-Donders, P., and Pantz, O., 2019, "Topology Optimization of Modulated and Oriented Periodic Microstructures by the Homogenization Method," Comput. Math. Appl., **78**(7), pp. 2197–2229.
[14] Groen, J. P., Stutz, F. C., Aage, N., Bærentzen, J. A., and Sigmund, O., 2020, "De-homogenization of Optimal Multi-scale 3D Topologies," Comput. Methods Appl. Mech. Eng., **364**, p. 112979.
[15] Geoffroy-Donders, P., Allaire, G., and Pantz, O., 2020, "3-D Topology Optimization of Modulated and Oriented Periodic Microstructures by the Homogenization Method," J. Comput. Phys., **401**, p. 108994.
[16] Stutz, F. C., Groen, J. P., Sigmund, O., and Bærentzen, J. A., 2020, "Singularity Aware De-homogenization for High-Resolution Topology Optimized Structures," Struct. Multidiscipl. Optim., **62**, pp. 2279–2295.
[17] Groen, J. P., Wu, J., and Sigmund, O., 2019, "Homogenization-Based Stiffness Optimization and Projection of 2D Coated Structures With Orthotropic Infill," Comput. Methods Appl. Mech. Eng., **349**, pp. 722–742.
[18] Wu, J., Wang, W., and Gao, X., 2021, "Design and Optimization of Conforming Lattice Structures," IEEE Trans. Vis. Comput. Graph., **27**(1), pp. 43–56.
[19] Stutz, F. C., Olsen, T. F., Groen, J. P., Aage, N., Sigmund, O., Solomon, J., and Bærentzen, J. A., 2022, "Synthesis of Frame Field-Aligned Multi-laminar Structures," ACM Trans. Graph., **41**(5), pp. 1–20.
[20] Elingaard, M. O., Aage, N., Bærentzen, J. A., and Sigmund, O., 2022, "De-Homogenization Using Convolutional Neural Networks," Comput. Methods Appl. Mech. Eng., **388**, p. 114197.
[21] Lee, J., Kwon, C., Yoo, J., Min, S., Nomura, T., and Dede, E. M., 2021, "Design of Spatially-Varying Orthotropic Infill Structures Using Multiscale Topology Optimization and Explicit De-Homogenization," Addit. Manuf., **40**, p. 101920.
[22] Zhu, Y., Li, S., Du, Z., Liu, C., Guo, X., and Zhang, W., 2019, "A Novel Asymptotic-Analysis-Based Homogenisation Approach Towards Fast Design of Infill Graded Microstructures," J. Mech. Phys. Solids, **124**, pp. 612–633.
[23] Kratz, A., Schoeneich, M., Zobel, V., Burgeth, B., Scheuermann, G., Hotz, I., and Stommel, M., 2014, "Tensor Visualization Driven Mechanical Component Design," IEEE Pacific Visualization Symposium, Yokohama, Japan, Mar. 4–7.
[24] Kwok, T.-H., Li, Y., and Chen, Y., 2016, "A Structural Topology Design Method Based on Principal Stress Line," Comput.-Aided Des., **80**, pp. 19–31.
[25] Wang, J., Wu, J., and Westermann, R., 2022, "Stress Trajectory Guided Structural Design and Topology Optimization," International Design Engineering Technical Conferences and Computers and Information in Engineering Conference, St. Louis, MO, Aug. 14–17.
[26] Loos, S., Wolk, S. v. d., Graaf, N. d., Hekkert, P., and Wu, J., 2022, "Towards Intentional Aesthetics Within Topology Optimization by Applying the Principle of Unity-in-Variety," Struct. Multidiscipl. Optim., **65**(7), p. 1851.
[27] Wu, J., Sigmund, O., and Groen, J. P., 2021, "Topology Optimization of Multi-scale Structures: A Review," Struct. Multidiscipl. Optim., **63**(3), pp. 1455–1480.
[28] Wang, J., Neuhauser, C., Wu, J., Gao, X., and Westermann, R., 2022, "3D-TSV: The 3D Trajectory-Based Stress Visualizer," Adv. Eng. Softw., **170**, p. 103144.
[29] Wang, J., Wu, J., and Westermann, R., 2022, "Stress Topology Analysis for Porous Infill Optimization," Struct. Multidiscipl. Optim., **65**(3), pp. 1–13.
[30] Delmarcelle, T., and Hesselink, L., 1994, "The Topology of Symmetric, Second-Order Tensor Fields," Proceedings Visualization'94, Washington, DC, Oct. 21, IEEE, pp. 140–147.
[31] Wu, J., Aage, N., Westermann, R., and Sigmund, O., 2018, "Infill Optimization for Additive Manufacturing – Approaching Bone-Like Porous Structures," IEEE Trans. Vis. Comput. Graph., **24**(2), pp. 1127–1140.
[32] Gao, X., Jakob, W., Tarini, M., and Panozzo, D., 2017, "Robust Hex-Dominant Mesh Generation Using Field-Guided Polyhedral Agglomeration," ACM Trans. Graph., **36**(4), pp. 114:1–114:13.